Journal of the European Ceramic Society 19 (1999) 2797–2814

PII: S0955-2219(99)00079-5
0955-2219/99/$ - see front matter

High Temperature Deformation of Precursor-derived Amorphous Si–B–C–N Ceramics

B. Baufeld, [a]* H. Gu, [c] J. Bill, [b] F. Wakai [c] and F. Aldinger [a,b]

[a]Max-Planck-Institut für Metallforschung, Stuttgart, Germany
[b]Institut für Nichtmetallische Anorganische Materialien, Universität Stuttgart, Germany
[c]Ceramics Superplasticity Project, ICORP, Japan Science and Technology Corporation (JST), Nagoya, Japan

(Received 1 September 1998; accepted 13 March 1999)

Abstract

The deformation of amorphous Si–B–C–N ceramics derived from polymeric boron-containing polysilylcarbodi-imide was investigated at temperatures between 1500 and 1700°C in nitrogen atmosphere. The composition of the as-thermolysed ceramic was determined to be $SiB_{0.41\pm0.11}C_{3.39\pm0.44}N_{2.42\pm0.31}O_{0.22\pm0.14}$ *and no remarkable change was observed after testing at 1600°C in nitrogen atmosphere. Under uniaxial compression a true strain of more than 30% was achieved without visible damage. By compression at constant strain rate a maximum densification of 26% was achieved. Besides densification non-Newtonian viscous flow was observed with an apparent activation energy of 0·8 MJ* mol^{-1} *and an apparent activation volume between 2·5 and 0·2* nm^3*. A free volume in the same order of a few cubic nanometers was assumed. At 1600°C the amorphous ceramic starts to crystallize with a volume fraction of crystalline phase less than 10% after several hours. The apparent increase in stress during deformation was explained by changes in sample size, porosity and intrinsic structure due to a decrease in free volume.* © *1999 Elsevier Science Ltd. All rights reserved*

Keywords: precursors-organic, porosity, mechanical properties, plasticity, amorphous ceramics, Si–B–C–N.

1 Introduction

Amorphous precursor-derived ceramics based on covalent bond forming elements such as Si, B, C and/or N promise to have high thermal, chemical and mechanical stability due to the lack of grain boundaries and oxide-type secondary phases. Despite some work in the early 1960s[1] the potential of such glass-type materials was not recognized until Yajima and co-workers, as well as Veerbeck and Winter prepared silicon nitride and silicon carbide-based ceramic fibers.[2–7] Since then, numerous pre-ceramic compounds for the synthesis of non-oxide ceramics have been developed yielding fibers, thin films and bulk bodies as well.[8–22]

Recently, preliminary information relating to the high temperature mechanical properties of precursor-derived materials has been published.[23–28] It is the object of this paper to report on the deformation behavior of the glass-type materials in more detail and to investigate possible deformation mechanisms.

For the micromechanisms of the viscous flow of glasses[29,30] different models have been proposed. Gilman[31] postulated the existence of dislocations with Burgers vectors that fluctuate along the dislocation line. However, in glasses where no long range translational order exists, the appearance of line defects is very unlikely. Another model, based on computer modeling, suggests that sites with extreme values of shear stress, so-called τ-defects, play a major role in the plastic deformation.[30] Furthermore, the free volume theory[32,33] has also been adopted to describe the micromechanisms of the plastic flow.[34] In this approach it is assumed that local shear is produced by atomic jumps in the regions of large free volume, and in the steady state, a dynamic equilibrium is maintained between the stress driven diffusional creation and annihilation of the free volume. However, due to the lack of long range order in amorphous material, direct experimental evidence, such as that provided by electron microscopy, is hard to obtain for one or the other model.

* To whom correspondence should be addressed at present address: European Commission, Joint Research Centre, Institute for Advanced Materials, PO Box 2, NL-1755 ZG Petten, The Netherlands.

2 Preparation and Characterization of the Material

2.1 Synthesis and thermolysis

The Si–B–C–N ceramics investigated were produced by thermolysis of boron-modified polysilylcarbodiimide. This precursor was synthesized by the reaction of hydroborated vinylchlorosilane with an excess of bis(trimethylsilyl)carbodi-imide (Bis):[35]

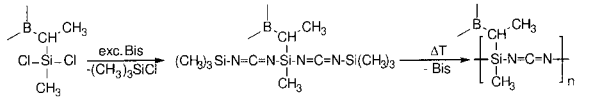

(1)

This reaction route which has been considered to be the first non-oxide sol–gel process for the synthesis of Si–B–C–N precursors results in an oxygen-sensitive brittle resin-like product, which can be ground into powder by attrition milling in an inert atmosphere (N2). Such powder was densified by 'plastic forming' in a graphite die[36] by first subjecting it to a pressure of about 30 MPa and then heating under pressure at 7·5 K min^{-1} up to temperatures between 148 and 150°C. After 10 min the green body was cooled by the same temperature ramp and then unloaded. Subsequently, the obtained green body was converted into ceramic monoliths by heating at 1 K min^{-1} up to 1400°C in argon atmosphere and thermolysing for 2 h. Thermogravimetric analysis of the as-thermolysed product in nitrogen atmosphere showed thermal stability up to at least 1600°C and a mass loss of about 30% starting at 1700°C.[37]

2.2 Composition, structure and phase equilibria

According to chemical analysis the amorphous as-thermolysed ceramic has a composition of 31·3 wt% Si, 4·7 wt% B, 34·6 wt% C, 27·0 wt% N and 3·5 wt% O (M. Christ, pers. comm.) (the respective values in at% are shown in Table 1). The concentration of Si and B was determined by Fourier-transform infrared spectrometry (Fluorine Volatilization-FTIRS) and optical emission spectrometry with an inductively coupled plasma (OES–JCP).[38] The concentration of N and O was determined by the carrier gas hot extraction procedure in which N is extracted from the sample at about 2500°C and transported by a carrier gas (He) to the thermal conductivity detector (TCD). O reacts with C to CO which is oxidized to CO_2. This is detected in an infrared absorption cell. For the determination of the C concentration after combustion of the sample the same procedure was applied.

The chemical composition was measured also by electron energy loss spectrometry (EELS) with a parallel EELS spectrometer and a dedicated scanning transmission electron microscope (STEM) from areas of 10×10 nm^2 or 20×20 nm^2. The atomic ratio of any two elements was calculated from the ratio of their edge intensities normalized by corresponding cross-sections.[39] The composition can be obtained after the ratios for all elements are achieved. A typical spectrum is shown in Fig. 1; the background signal underneath the Si-*L* edge has been subtracted. Although the Si–$L_{2,3}$, Si–L_1, B–*K*, C–*K* and N-*K* edges are all clearly visible, the O–*K* edge is much weaker due to both the lower concentration and the lower inelastic cross-section. The inset of Fig. 1 gives the derivative spectral form for the O–*K* edge, together with that for the N–*K* edge for comparison. The visibility of the O–*K* edge has been increased in its derivative form. No evidence for H was found. After averaging over eight measurements from different regions, the composition of the as-thermolysed Si–B–C–N material is determined to be $SiB_{0.41\pm0.11}C_{3.39\pm0.44}N_{2.42\pm0.31}O_{0.22\pm0.14}$. The standard deviations are also given in this formula. It is noteworthy, that within the limit of error the results from the chemical analysis and the EELS measurements correspond (see Table 1).

Neglecting the O concentration and normalizing the data of the chemical analysis to 100% gives a composition of 17·6 at% Si, 6·3 at% B, 45·6 at% C and 30·5 at% N ($SiB_{0.36}C_{2.59}N_{1.73}$). According to the Si–B–C–N phase diagram at temperatures up to 1484°C this composition (indicated in Fig. 2 by ■) is very close to the three-phase equilibrium graphite + BN + Si_3N_4 with a small amount of gas

Table 1. Compositions of Si–B–C–N materials measured by chemical analysis and by EELS

Sample	*No of measurements by EELS*	*Si at%*	*B at%*	*C at%*	*C at% (cat./an.)*[a]	*N at%*	*O at%*
As-thermolysed[b]	—	17·0	6·1	44·1	23·2/21·0	29·5	3·3
As-thermolysed[c]	8	13·4	5·6 ± 1·5	45·6 ± 5·9	26·9/18·7	32·5 ± 4·2	3·0 ± 1·8
1500°C[c]	4	15·1	6·5 ± 2·6	47·5 ± 13·6	25·1/22·4	28·7 ± 1·9	2·2 ± 1·0
(1500°C)[c,d]	3	16·2	7·3 ± 3·2	43·7 ± 1·7	22·9/20·8	29·9 ± 1·2	2·8 ± 0·6
1600°C[c]	7	12·9	5·6 ± 2·8	49·7 ± 22·7	27·9/21·8	29·2 ± 7·5	2·5 ± 0·9
(1600°C)[c,d]	5	15·8	5·0 ± 1·0	45·2 ± 6·1	25·2/20·0	31·4 ± 5·8	2·6 ± 0·9

[a] Percentage of C in cation or anion states estimated from the overall stoichiometry. See more details in the text.
[b] Data obtained from chemical analysis.
[c] Data obtained by EELS.
[d] Data chosen to exclude large scatters, especially the ones with high C content which may be caused by the emerging of the graphite-based crystalline.

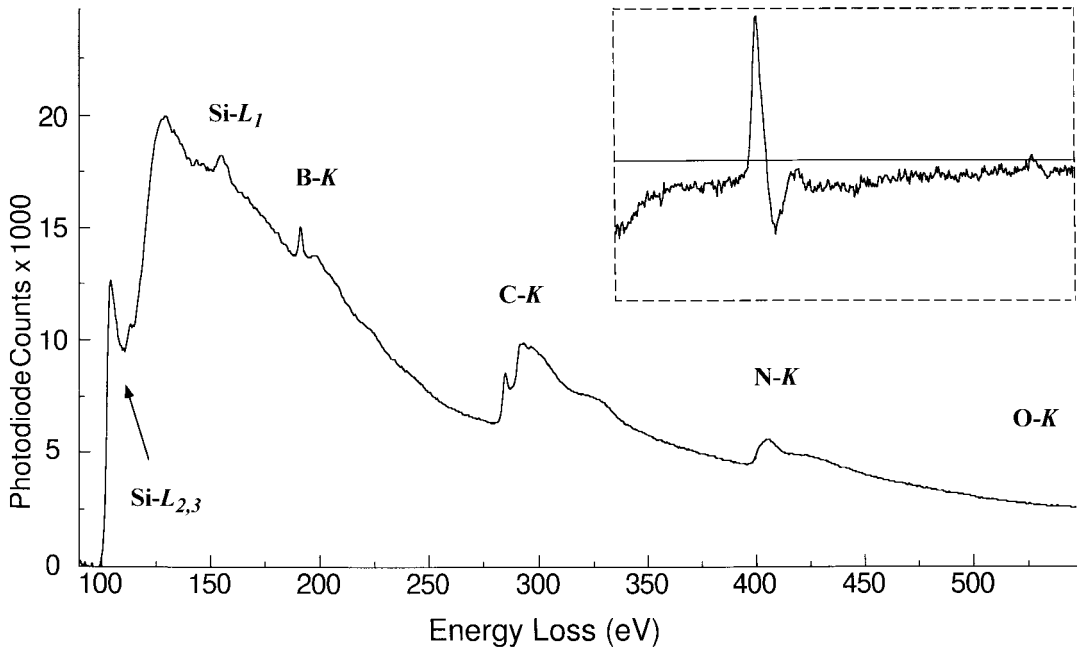

Fig. 1. EELS spectrum of as-thermolysed Si–B–C–N material showing the presence of all these elements. The inset shows the weak presence of O revealed by the derivative spectral form in the difference spectrum.

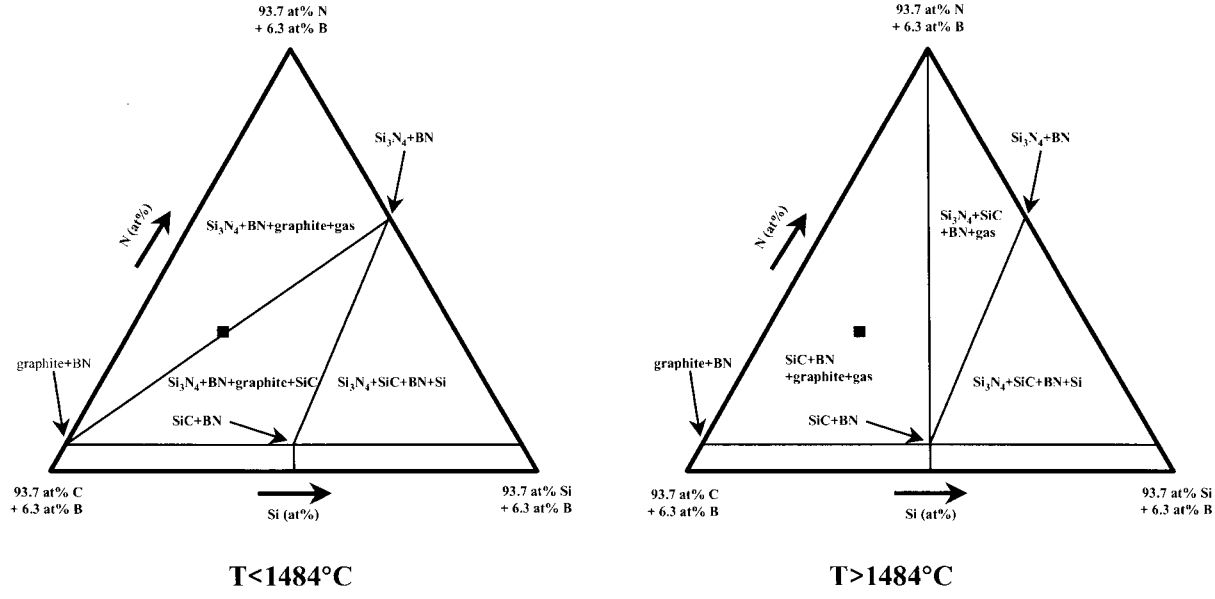

Fig. 2. Isothermal section of the quaternary Si–B–C–N system with 6·3 at% B below and above 1484°C. The composition of the ceramic according to chemical analysis—normalized excluding O—is indicated by ■.

phase. The relative amounts of the phases at this composition can be seen from Fig. 3 (Refs 40, 41; J. Peng and M. Seifert, pers. comm). Above 1484°C the Si_3N_4 reacts with C according to

$$Si_3N_4 + 3C \rightarrow 3SiC + 2N_2 \quad (2)$$

Therefore, at thermal equilibrium above 1484°C the three-phase system SiC + BN + graphite is expected (see Fig. 3). The relative phase-amount of graphite is reduced and the system will release gas consisting mostly of nitrogen. Interestingly, the BN phase does not take part in the invariant phase reaction; thus the absolute relative phase-amount of BN does not change. It is important to note that these considerations of the phase equilibria do not tell anything about the time for reaching the equilibria.

The as-thermolysed material is amorphous according to X-ray investigations. After deformation tests at 1500°C the material still is X-ray amorphous. However, for samples deformed at 1600°C frequently weak broad X-ray diffraction patterns can be detected, as shown in Fig. 4, indicating the beginning of crystallization. It is believed that these reflections are due to a small volume fraction of nano-sized crystallites. Testing at 1700°C or heat-treatment at 1800°C has resulted in distinct X-ray diffraction patterns typical for crystalline SiC.

Reflections of other crystalline phases were not found.

2.3 Microstructure and density

The microstructure of as-thermolysed material is shown in Fig. 5. It exhibits substantial inhomogeneities. At low-magnification [Fig. 5(a)] dark, large elliptical areas with dimensions in the order of several hundred microns, bright areas of irregular shape with dimensions in the order of a few tens of microns and small uniformly distributed dark spots can be differentiated. The bright areas are dense material as evidenced by the detailed view in Fig. 5(b). The dark contrast represents pores. Therefore, the material consists of mainly three different areas distinguished by their porosity, namely dense areas (bright structures with irregular shape), very porous areas (elliptical dark structures) and a matrix with medium porosity. Digital analysis of the images of the polished surface of as-thermolysed samples, such as in Fig. 6(a), results in an average pore cross section of about 5 μm^2 and a relative surface fraction of the pores of about 22%.

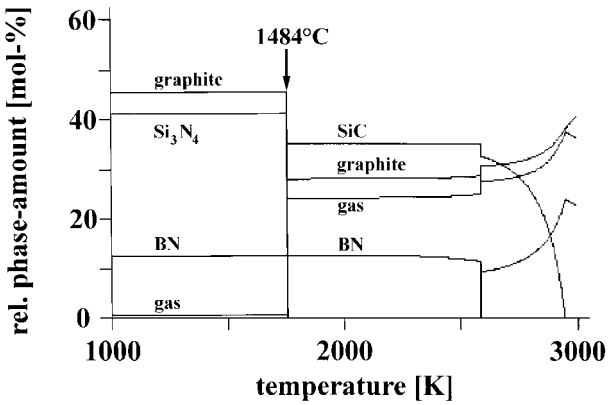

Fig. 3. Phase fraction diagram of the Si–B–C–N system with 17·6 at% Si, 6·3 at% B, 45·6 at% C and 30·5 at% N at 1 bar according to J. Peng and H. Seifert (pers. comm.).

The apparent density of the as-thermolysed material—including open and closed pores—is about 1·64 g cm^{-3}. Helium porosimetry on the bulk material, which gives the density of the material including the closed pores, resulted in 1·93 g cm^{-3}. Using the result of Helium porosimetry of fine ground powder the density of pore free material was estimated to be equal to 2·1 g cm^{-3} (M. Christ, pers. comm.). These results reveal an open porosity of 15% and a closed porosity of 7%, i.e. a total porosity of 22%. This result correlates with the porosity value gained by image analysis (see above). It is also in approximate agreement with the densification of the material by uniaxial compression with which—as will be shown later—a maximum density of 2·04 g cm^{-3} (at $\varepsilon_{true} = 35\%$) and a porosity decrease from 22% to 3% at 1600°C was observed.

The relative amount of the free volume in the pore free material can be estimated by comparing its density (2·1 g cm^{-3}) with the density of a hypothetical crystalline material having the same composition ($SiB_{0.36}C_{2.59}N_{1.73}$) and consisting of the crystalline phases Si_3N_4, BN and graphite (2·68 g cm^{-3}). This gives 22% relative amount of free volume.

The intrinsic structure was studied with STEM/EELS. The contrast in STEM bright field (BF)

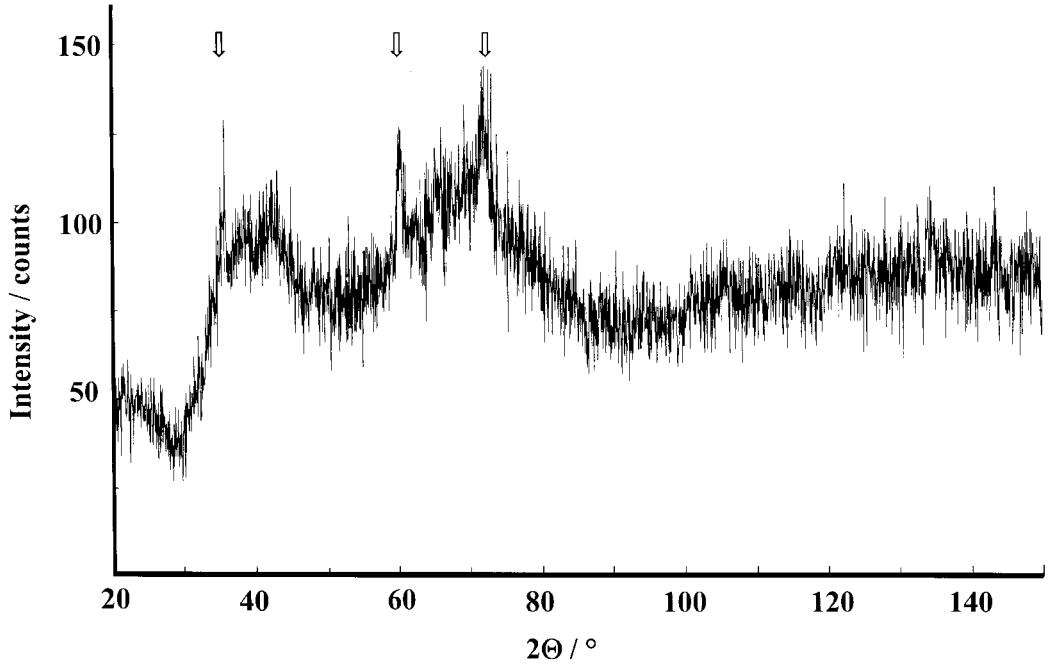

Fig. 4. X-ray spectrum of a sample deformed at 1600°C for $\varepsilon_{true} = 18\%$ with 4×10^{-5} 1/s. The arrows indicate the position of the major X-ray reflections of β-SiC.

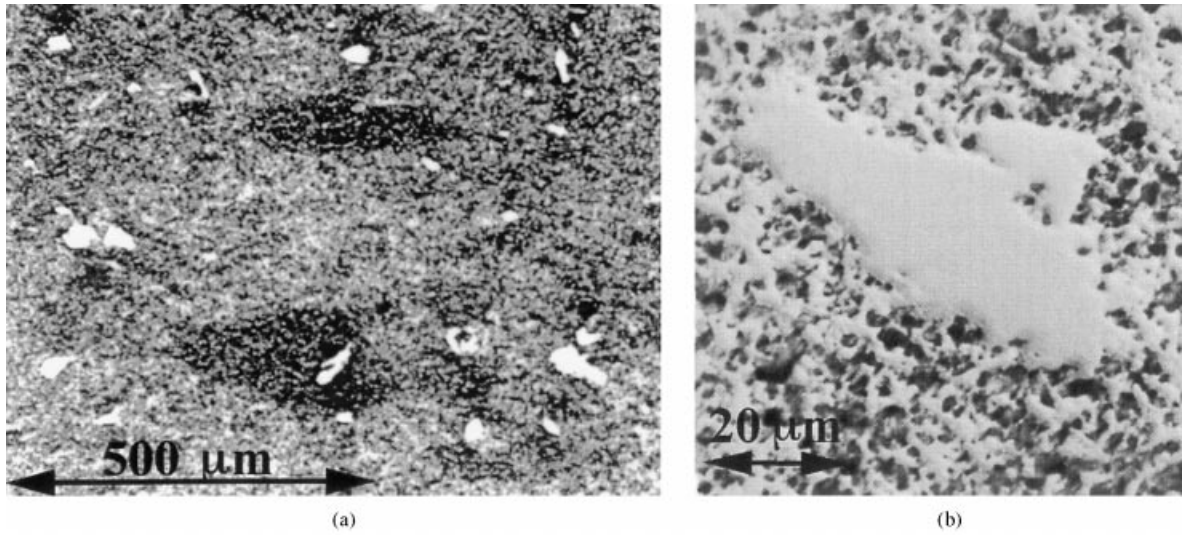

Fig. 5. Optical micrographs of the polished surface of as-thermolysed precursor-derived Si–B–C–N ceramics at different scales, viewed perpendicular to the plastic forming direction.

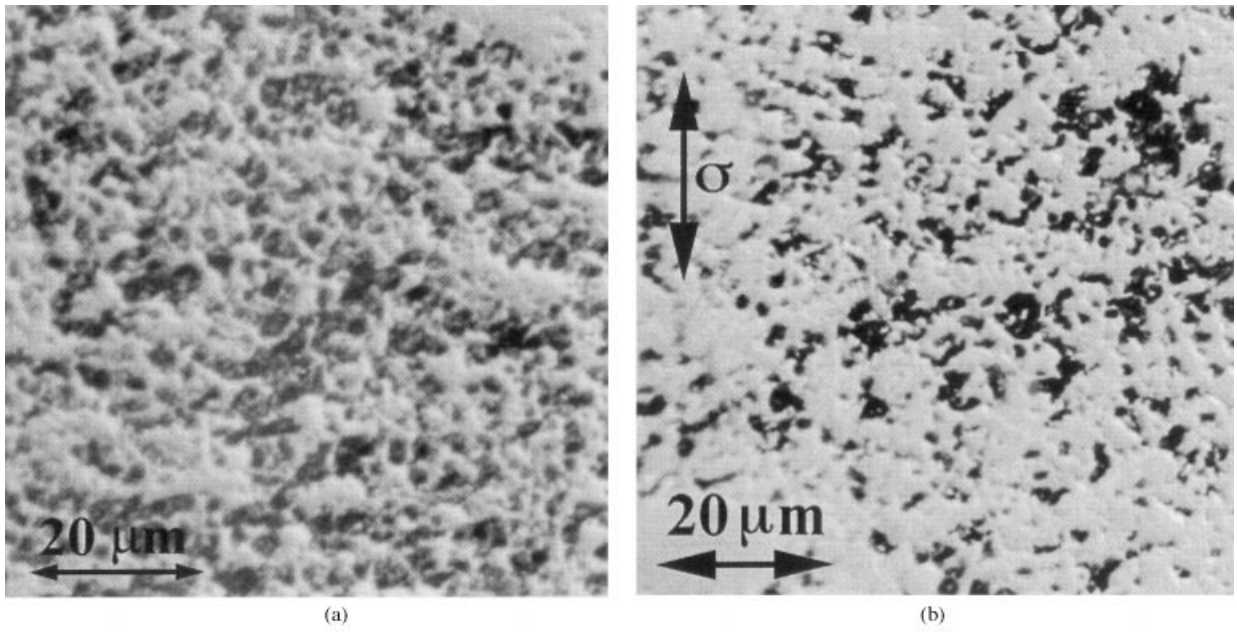

Fig. 6. Optical micrographs of the polished surface of (a) an as-thermolysed precursor-derived Si–B–C–N ceramic and (b) of material deformed at 1500°C for 7% with 1×10^{-5} 1/s ($\updownarrow\ \sigma$ indicates compression direction).

images is equivalent to phase contrast in the images of the conventional TEM through the so-called 'reciprocal theorem'.[42] The phase contrast is sensitive to the structure of the analyzed areas as well as to the defocus value of the objective lens;[43] thus the structure of the amorphous materials can be directly seen. On the other hand, the contrast in high-angle annular dark-field (HADF) images is more sensitive to the atomic number of the scattering elements since scattering to high angle is essentially of the individual nature and the correlation between scattering atoms in the solid is largely reduced. It is often referred to as 'Z-contrast' due to its direct relation with the atomic number Z.[44]

STEM specimens were prepared by crushing the bulk samples in acetone with pestle and mortar. The resulted small pieces were caught on using TEM grids covered with holey carbon films. In this way the irradiation damage from the ion milling is avoided.

The structure of the amorphous precursor-derived Si–B–C–N materials is homogeneous at the atomic scale, as shown in a phase-contrast STEM BF image [Fig. 7(a)]. However, a 'Z-contrast' image of the identical area [STEM HADF image in Fig. 5(b)] is in strong contrast with the BF image: high inhomogeneity with white features of 1 to 5 nm are visible. Because of the absence of any distinctively

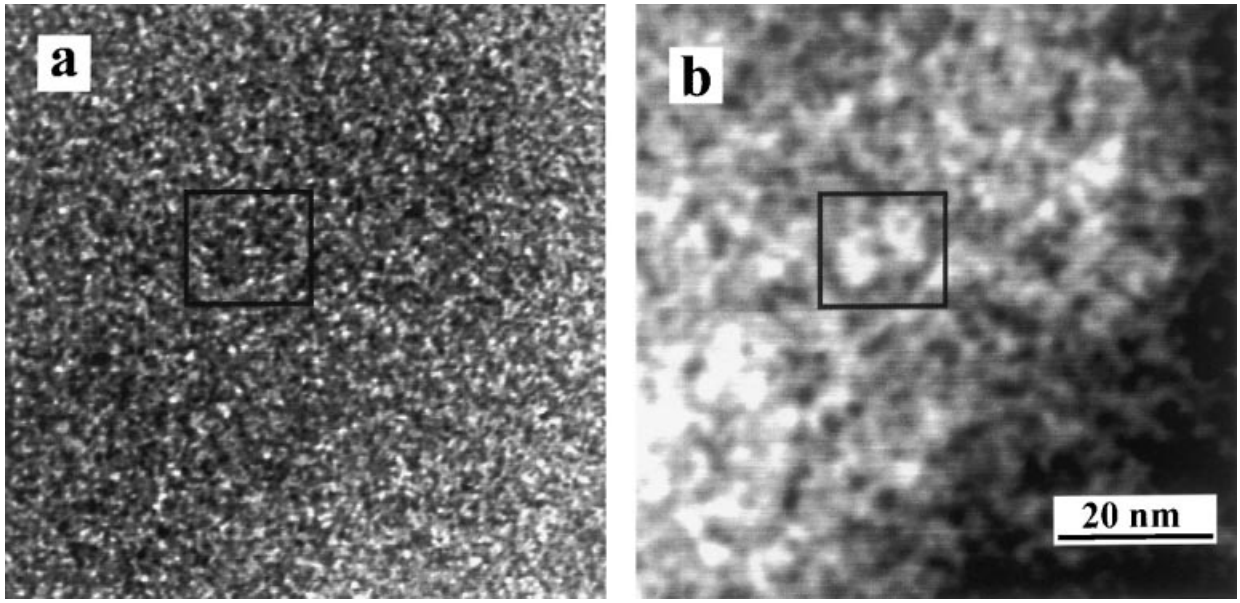

Fig. 7. STEM BF (a) and HADF (b) images of precursor-derived Si–B–C–N material deformed at 1500 C for 3 h in N atmosphere. Squares mark two clusters which show different contrast in the two images.

heavy element in the amorphous material, such contrasts must come mainly from density variations. Brighter contrast corresponds to dense areas, i.e. the clustered areas. The dark contrasts arise from less dense areas. This structure might be related to phase separated regions similar to those found in precursor-derived ternary Si–C–N material[45–47] or to the free volume between clusters. Subsequent changes of the focus give strong evidence for the latter case. Such density variation is also reflected in the BF-image of Fig. 7(a): although the phase-contrast dominates, the dense areas appear slightly darker due to the stronger absorption of the electrons. The two dark regions in the squares in Fig. 7—which mark the same area in both images—correspond to two large clusters.

2.4 Mechanical testing

The mechanical properties of the material were investigated by compression tests of rectangular specimens of $2\times2\times3$ mm^3. The compression direction was parallel to the plastic forming direction (see Section 2.1). The samples were cut by a tungsten wire saw using SiC powder, ground with a diamond wheel and polished with diamond abrasive of 3 μm grain size on polishing cloth. Oil was always used as lubricant in order to avoid oxygen contamination from water. After polishing, the specimens were heat-treated for one hour at 1000°C in nitrogen atmosphere in order to remove the oil from the porous material. The samples were deformed in compression at constant strain rate at temperatures in the range of 1500 to 1700°C in nitrogen atmosphere using a hydraulic Shimazu Servopulser testing machine. The heating was performed via induction heating using a tungsten susceptor. A heating rate of 50 K min^{-1} was used except for the last 100 K where the samples were heated at 20 K min^{-1}. At the final temperature the samples were held for about 30 min to reach thermal equilibrium.

The compression stress σ was calculated as the ratio of actual load and original cross section A_0. The engineering strain and the true strain $\varepsilon_{\text{true}}$ were calculated as

$$\varepsilon = 1 - l/l_0 \tag{3a}$$

$$\varepsilon_{\text{true}} = |ln(l/l_0)| \tag{3b}$$

with the original sample length l_0 and the actual length l.

Frequently, the correlation between plastic strain rate $\dot{\varepsilon}_{\text{plast}}$ and flow stress σ is described phenomenologically by a power law

$$\dot{\varepsilon}_{\text{plast}} = A\sigma^n \exp(-Q/kT), \tag{4}$$

where A is a constant, n the stress exponent, Q the apparent experimental activation energy, k the Boltzmann factor and T the absolute temperature. Another description for the relation between strain rate and stress is given by the Arrhenius-type relationship[48]

$$\dot{\varepsilon}_{\text{plast}} = \dot{\varepsilon}_0 \exp(-\Delta G(\sigma)/kT). \tag{5}$$

The pre-exponential factor $\dot{\varepsilon}_0$ is usually considered to be constant and $\Delta G(\sigma)$ is the activation Gibbs free energy, which in general is stress dependent. Based on eqns (3) and (4) the stress exponent n, the strain rate sensitivity of the flow stress I and the

activation enthalpy ΔH were determined according to the following formulas:[48]

$$n = \frac{\partial(ln\dot{\varepsilon}_{\text{plast}})}{\partial(ln\sigma)}|_T, \tag{6}$$

$$I = \frac{\partial\sigma}{\partial(ln\dot{\varepsilon}_{\text{plast}})}|_T \tag{7}$$

and

$$\Delta H = Q = -\frac{kT^2}{I}\left(\frac{\partial\sigma}{\partial T}\right)|_{\dot{\varepsilon}} \tag{8}$$

The strain rate sensitivity I is related to the activation volume of a thermally activated process V by:[48]

$$V = \frac{kT}{m_{\text{SF}}I}. \tag{9}$$

The Schmid factor m_{SF} is a geometric factor which is 0·5 for the isotropic case. The stress exponent n and the strain rate sensitivity I are determined with stress relaxation tests. In such tests, at a constant strain rate the strain is suddenly held constant and the decrease of stress is measured.

Due to Hook's law the total strain rate $\dot{\varepsilon}_{\text{total}}$ can be expressed by

$$\dot{\varepsilon}_{\text{total}} = \dot{\varepsilon}_{\text{plast}} + \dot{\varepsilon}_{\text{elast}} = \dot{\varepsilon}_{\text{plast}} + \dot{\sigma}/E, \tag{10}$$

where E is the elastic modulus of specimen and testing machine. In stress relaxation experiments, i.e. at $\dot{\varepsilon}_{\text{total}} = 0$, the plastic strain rate $\dot{\varepsilon}_{\text{plast}}$ is proportional to the negative stress rate $-\dot{\sigma}$, which can be easily determined. The plotting of data from a stress relaxation test in the form of $\ln(-\dot{\sigma})$ versus σ in the following will be called relaxation curves. The inverse slope of such relaxation curves is equal to I. The slope of a plot of $\ln(-\dot{\sigma})$ versus $\ln(\sigma)$ gives n. Quite often such plots do not result in a linear dependence of the stress rate on stress indicating that eqn (4) is too simple. With these parameters and with the change in flow stress with temperature change, the apparent activation energy ΔH can be determined according to eqn (8).

3 Results and Interpretation

3.1 High-temperature stress–strain behavior

The amorphous precursor-derived Si–B–C–N ceramics can be deformed in compression by a large amount at high temperatures without perceptible sample damage. For example, the specimen shown in the optical micrograph in Fig. 8 was deformed at 1600°C for $\varepsilon_{\text{true}} = 41\%$. For comparison the original size of the sample is drawn schematically.

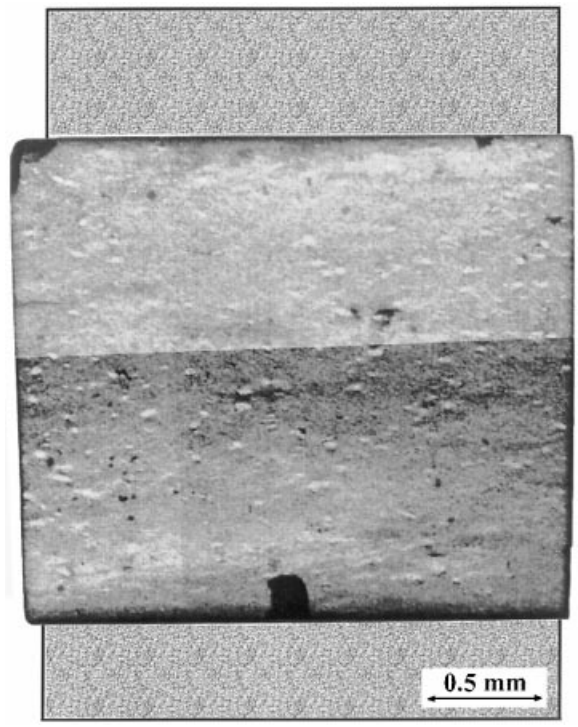

Fig. 8. Optical micrograph (assembled from two images) of a sample deformed at 1600°C with $\dot{\varepsilon} = 4 \times 10^{-5}$ 1/s for $\varepsilon_{\text{true}} = 41\%$. The original sample size is drawn schematically.

Typical stress–strain curves derived at 1500, 1600 and 1700°C are shown in Fig. 9. They show a sigmoidal shape with different deformation regimes: a regime at small strain with a strong almost linear increase of flow stress, followed by a regime with a decreasing slope, and at large strain a third regime in which the slope increases again. At 1700°C a mass loss of 23% occurred compared to the 6% usually observed in compression tests at 1600°C. Therefore, mechanical tests at 1700°C were not considered in detail.

In Fig. 10 the deformation behavior at 1500 and 1600°C is shown at different strain rates. At small strains the flow stress is almost linear with strain and independent of temperature and strain rate. In contrast, at higher strains the flow stress decreases with temperature (as in Fig. 9) and increases with strain rate.

A linear regime independent of temperature or strain rate is usually attributed to elastic deformation. However, as can be seen in Fig. 10, at fast unloading (+) the slope is much steeper than that at the first loading indicating elastic and plastic deformation taking place concurrently. As will be discussed in Section 3.3 by deformation the porosity of the samples is reduced. A decrease of porosity leads to an increase of the elastic moduli[49,50] which is the reason why at large strains the

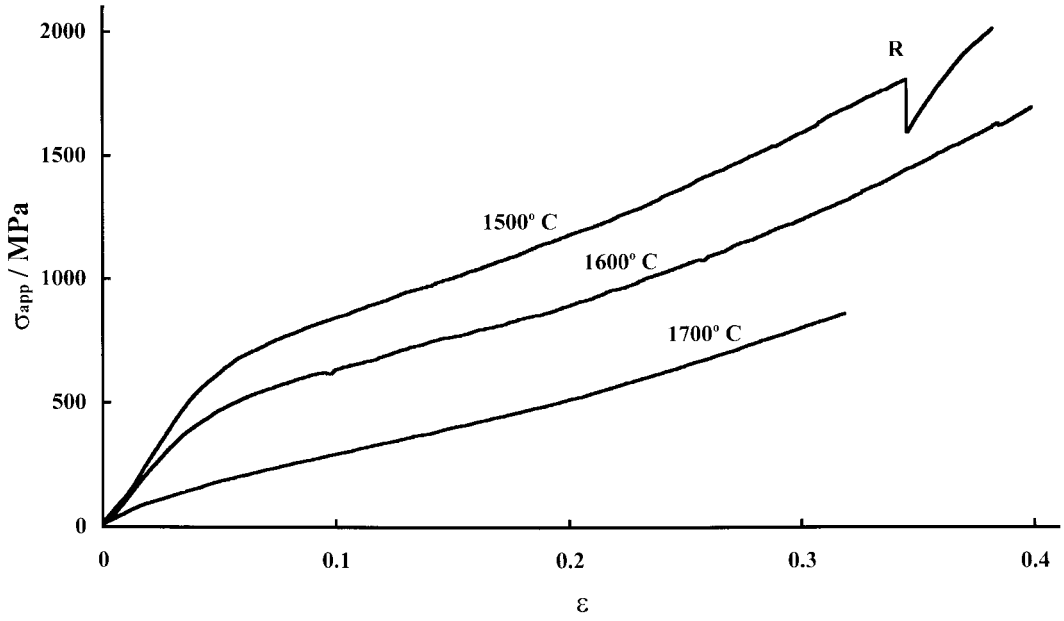

Fig. 9. Stress–strain curves of precursor-derived Si–B–C–N ceramics at a constant strain rate of $\dot{\varepsilon} = 4 \times 10^{-5}$ 1/s at 1500, 1600 and 1700°C, respectively. R identifies a stress relaxation experiment.

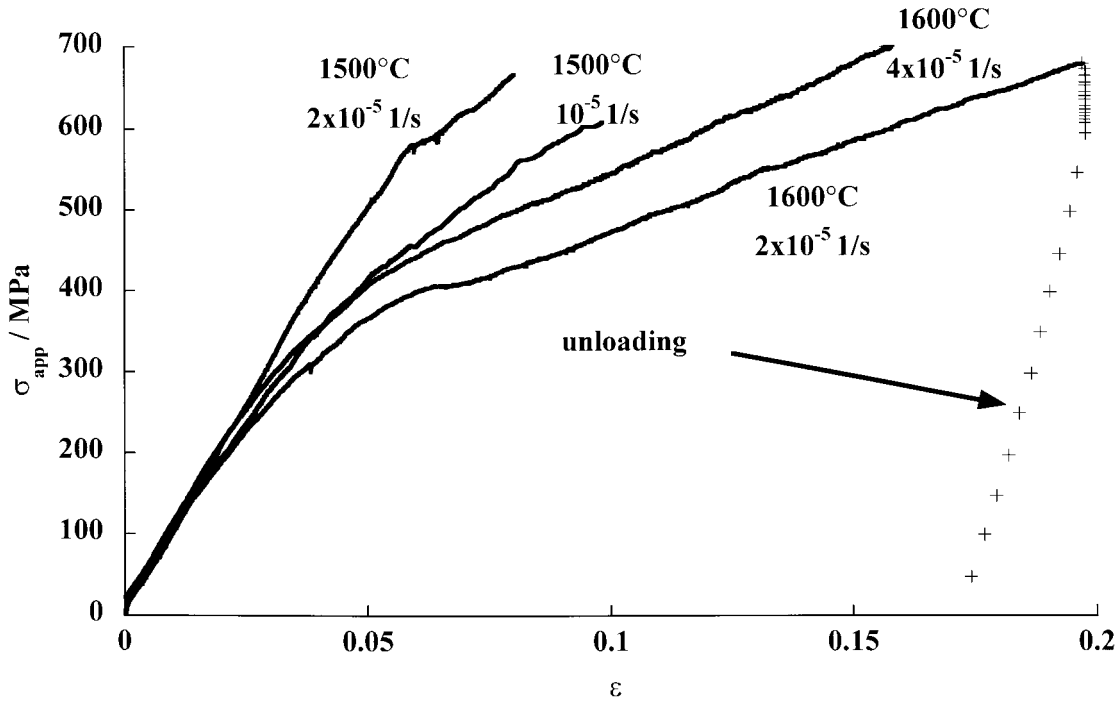

Fig. 10. Comparison of the stress-strain curves of precursor-derived Si–B–C–N ceramics deformed at various constant strain rates and temperatures including one fast unloading (+).

unloading curves are much steeper than the slopes at the first loading.

The strain rate sensitivity of the flow stress I and the stress exponent n were determined from stress relaxation experiments using eqns (6) and (7). In Figs 9 and 11 such stress relaxation experiments are designated with R. A typical example for a relaxation curve is given in Fig. 12. Stress relaxation curves usually are slightly concave at small strains and straight or slightly convex at higher strains. Data for I are shown in Fig. 13, which were calculated by determining the slope at values of high stress at the beginning of the stress relaxation test. It is evident that I increases with strain. At small strains I is independent of temperature. At higher strains it decreases with temperature.

The mean slopes of the relaxation curves were used to calculate the stress exponent n. The dependence of n on temperature or strain is similar to that of I: at small strain n has a value of about 2 and increases with strain to 4·7 at 1500°C and 4·2 at 1600°C at $\varepsilon_{\text{total}} \approx 34\%$. These values indicate non-Newtonian flow which is in opposition to Ref. 27. It is worthwhile to note that the plot $\ln(-\dot{\sigma})$

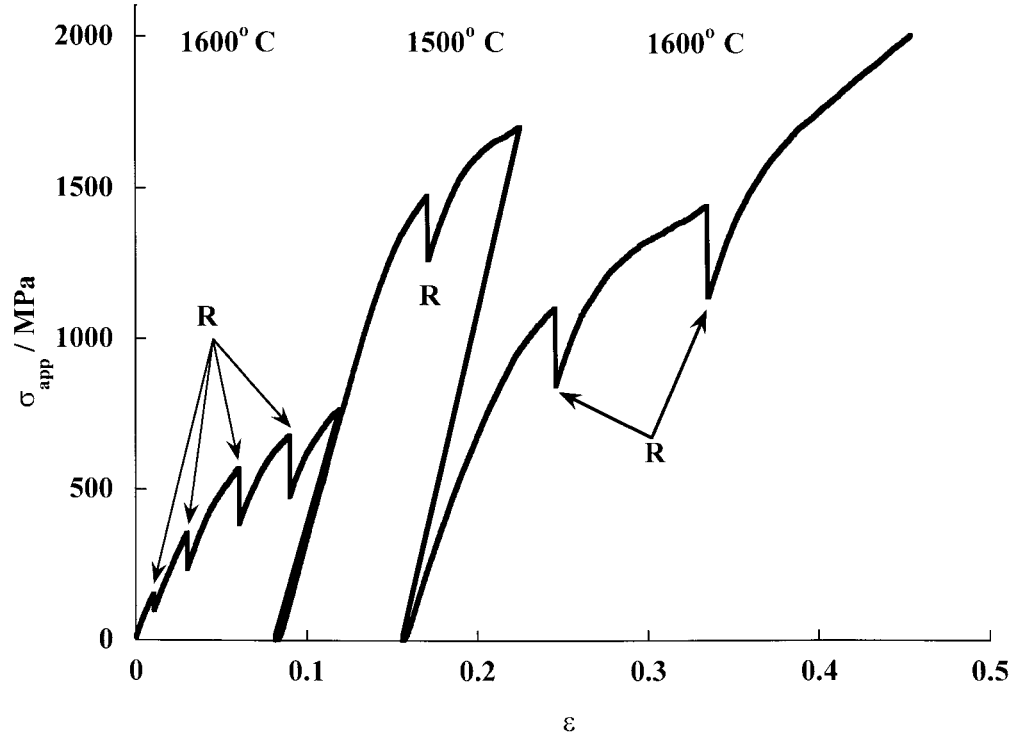

Fig. 11. Stress–strain curve of a specimen deformed at a constant strain rate of 4×10^{-5} 1/s including stress relaxation experiments (R) and temperature changes from 1600 to 1500°C and back to 1600°C.

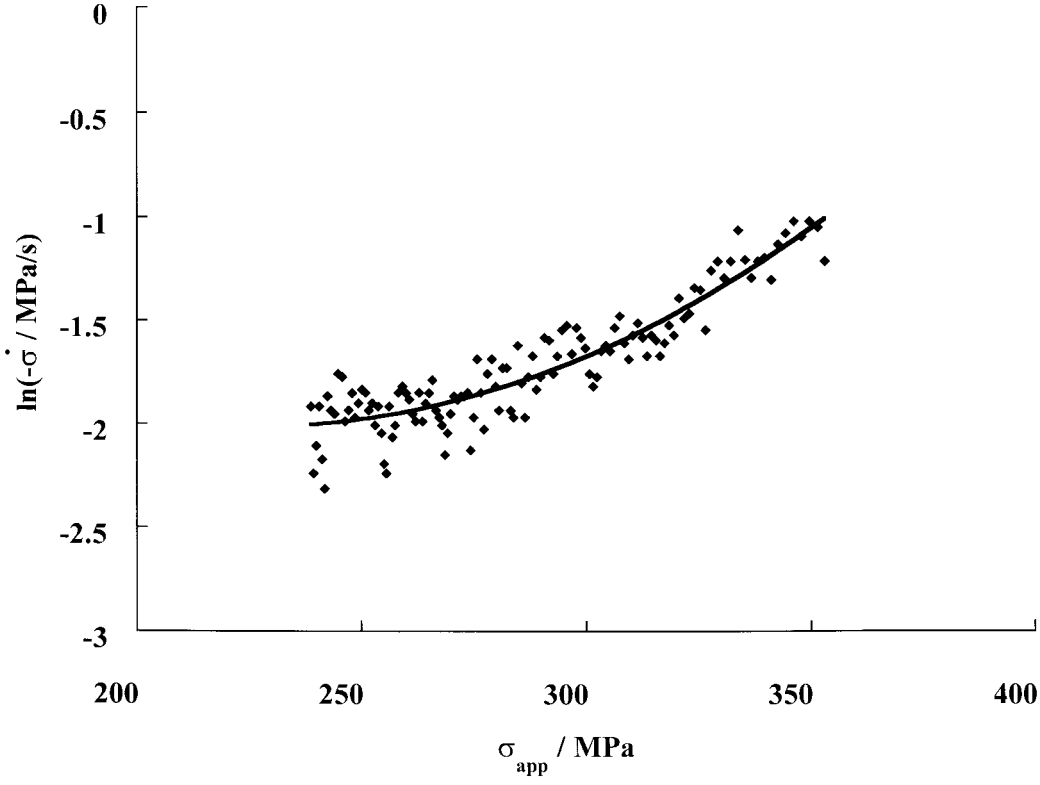

Fig. 12. Relaxation curve of a stress relaxation experiment at 1600°C at $\varepsilon = 9\%$.

versus $\ln(\sigma)$ is not linear in most cases. Therefore, it remains questionable whether eqn (4) can be applied and whether n is a useful parameter.

The apparent activation energy ΔH has been determined for two different samples with the following temperature sequences: 1600–1500–1600°C (Fig. 11) and 1500–1600–1500°C. Using a mean value of $\bar{I}$ from stress relaxation experiments before and after the temperature change and the resulting $\Delta\sigma$, ΔH was determined with eqn (8). Both measurements resulted in $\Delta H = 0{\cdot}8$ MJ mol^{-1}. This value is rather large and was determined at large strains. As already discussed at small strains the flow stress does not depend on temperature, hence

$\Delta H \approx 0$; in other words, the deformation in this regime is not a thermally activated process.

In order to compare the deformation behavior of pre-deformed with as-thermolysed material two pre-deformed compression samples were prepared. As shown in Fig. 14, pre-deforming increases the resistance to plastic deformation. Plastic deformation of the second run starts only at about the maximum stress of the first run; thus up to some 1 GPa the pre-deformed specimen exhibits only elastic deformation. After additional plastic deformation of about 5% failure took place for both pre-deformed samples at a stress as high as 1560 MPa, probably due to the high elastic energy stored in the sample.

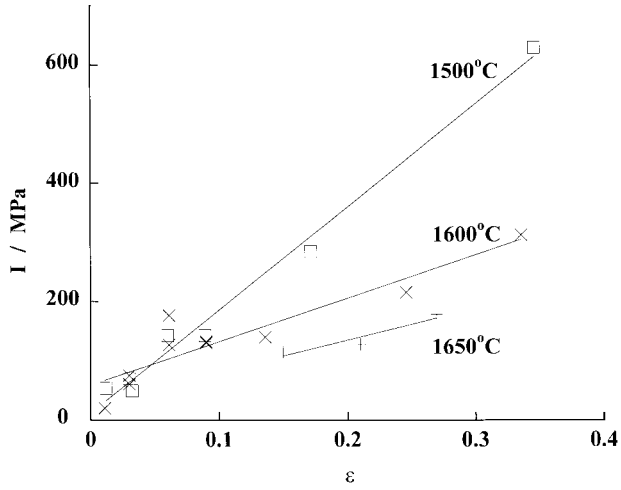

Fig. 13. Correlation between strain rate sensitivity I and strain ε at 1500°C (□), 1600°C (X) and 1650°C (+).

3.2 Development of the microstructure

According to EELS measurements the composition of the amorphous phase does not change significantly during compression tests at 1500 or 1600°C; the mean compositions for both samples tested are listed in Table 1.

A further look at the data in Table 1 reveals an increase in the deviation of C content with the deformation temperature. This is concurrent with the detection of small amounts of graphite phase at high temperature. The large deviation mainly resulted from a few measurements which gave excessively high carbon contents. It is highly possible that these measurements includes both the main amorphous Si–B–C–N phase and the secondary graphite-like phase. Indeed these carbon *K*-edge shapes are the linear combinations of the C–*K* edges from the main and the graphite phases. Excluding these data points, there is much less deviation in carbon content in the amorphous phase in both 1500 and 1600°C tested samples as well as slightly smaller C contents. These data from the selected measurements (excluding the high carbon content) are also listed in Table 1 (rows marked with superscript d).

As shown in Table 1 the Si content is relatively small compared to either C or N. Although the material is covalent in the general sense, the differences in electronegativity of these elements allows Si and B to be regarded as cations and N and O as anions. To maintain the nominal charge stoichiometry with the measured composition, carbon must then be divided into cations and anions

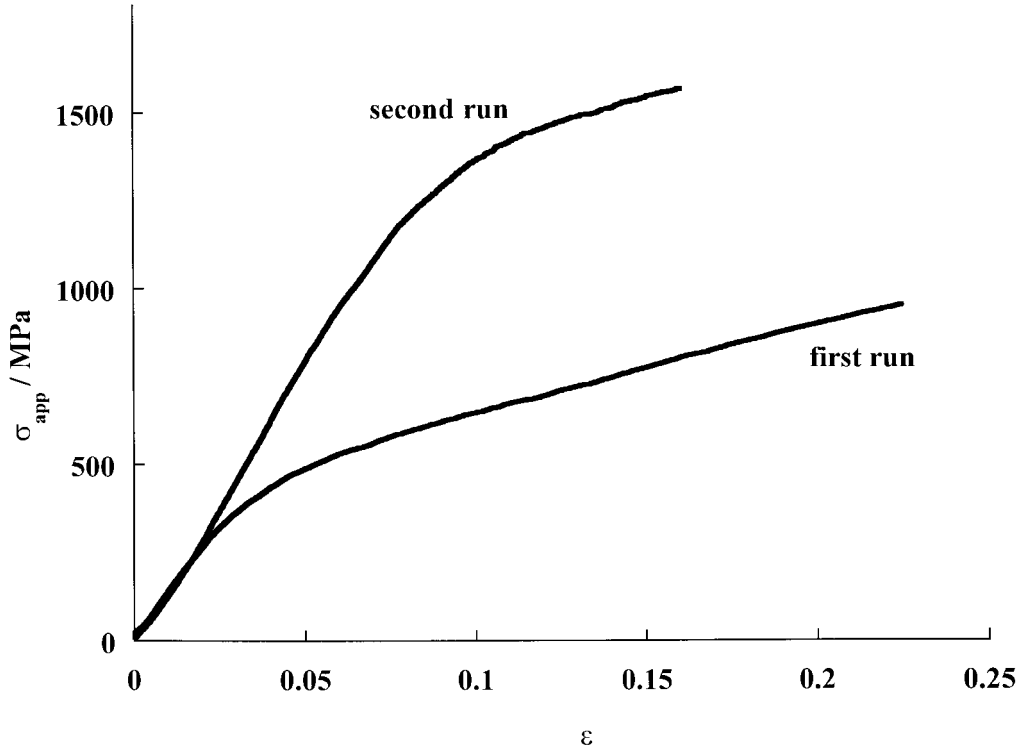

Fig. 14. Stress–strain curve of an as-thermolysed sample (first run) and of the second run after this experiment and after the re-preparation of a rectangular sample.

despite the fact that many form completely covalent C–C bonds. The contents of the cation-designated and the anion-designated carbon are also listed in Table 1 for each sample. It is surprising that carbon 'cations' always outnumber the carbon 'anions' The compression tests have a minor effect to reduce this gap. This large population of carbon 'cations' in the Si–B–C–N material opens the door to form the graphite phase at high temperatures where the mobility of atoms has been significantly enhanced. Even at the lower temperatures, C–C bonds are likely to be formed locally. This is the subject for future works. However, after all the carbon 'anions' have formed C–C bonds, there are still some carbon 'cations' remaining to form plausibly C–N bonds. Further evidence is necessary to verify the existence of such bonds. This can shed light into the structure and the stability of the amorphous Si–B–C–N.

It is known that heat treatment of amorphous precursor-derived Si–C–N ceramics lead to a phase separation with amorphous C and silicon nitride segregates.[45–47] A similar decomposition of the amorphous state of Si–B–C–N ceramics is very likely but has not been investigated yet.

The atomic structure of the Si–B–C–N material remains unchanged after deformation at temperature as high as 1500°C, which is consistent with X-ray diffraction. Crystallization starts at about 1600°C according to X-ray analysis which indicates the presence of a small amount of SiC (cf. Fig. 4). TEM investigations suggest that even after several hours at 1600°C the sample remains mostly amorphous and the volume fraction of crystal phase is less than 10% (H. Gu and B. Baufeld, unpublished results). By TEM observation and analysis besides the SiC crystallites, graphite regions and crystalline Si_3N_4 particles embedded in a mainly amorphous matrix were confirmed (H. Gu and B. Baufeld, unpublished results).

3.3 Densification

The porosity of the ceramic was decreased significantly by deformation as is evident when comparing the surfaces of the as-thermolysed sample [Fig. 6(a)] with that of a sample deformed for 7% [Fig. 6(b)]. In the latter case the pores contribute only 11% of the area. The deformation can be observed directly in Fig. 15, where the same sample area is shown before [Fig. 15(a)] and after compression [Fig. 15(b)]. The large dense areas conveniently act as markers. Despite the large deformation in the (vertical) compression direction, hardly any strain in the horizontal direction occurs. Close inspection of Fig. 15 reveals some flattening of pores perpendicular to the vertical compression direction. The increased surface roughness, seen in Fig. 15(b), most probably is related to the deleterious effect of the high testing temperature of 1600°C.

The dimensions of the samples were measured before and after the deformation experiments. In Fig. 16(a) the correlation between the relative change in sample width $\Delta w/w_0$ and $\varepsilon_{\text{true}}$ is plotted for the experiments at 1500 (□) and 1600°C (○). At constant sample volume the relation $\Delta w/w_0$ versus $\varepsilon_{\text{true}}$ should follow the solid line in this plot. However, the data show a much weaker dependence indicating a decrease in sample volume during deformation. Since at these temperatures the mass loss is 6% or less this decrease in sample volume must be attributed to densification. In Fig. 16(b) this increase in density with strain is shown. Apparently, the density increases almost linearly with $\varepsilon_{\text{true}}$. At $\varepsilon_{\text{true}} = 35\%$ the density is increased by 26%. The maximum density obtained by compression tests is 2·04 g cm^{-3}. In the temperature range investigated the densification seems not to depend on temperature.

At small strains $\Delta w/w_0$ is negative [Fig. 16(a)] indicating some shrinkage by sintering counteracting to some extend the increase in sample width during loading. At zero loading a heat treatment at 1600°C for 5 h in nitrogen atmosphere has led to a shrinkage of 3%. In the same way shrinkage was observed for as-thermolysed Si–C–N ceramics, derived from commercially available polyvinylsilazane when heated above the thermolysis temperature.[25,51]

Typical for compression loading is the concurrent occurrence of densification and plastic deformation. The separation of two different deformation mechanisms with one leading to a change in density has been suggested by Raj for tensile deformation[52] and later extended to the densification of powder compacts in compression.[53] At large strains it was suggested to use the concept of true strain, which at uniaxial deformation leads to the following equations:

$$|\varepsilon_{\text{dil}}| = |\varepsilon_{\text{true}} + 2\varepsilon_t| \tag{11}$$

$$\varepsilon_{\text{dev}} = \frac{2}{3}|\varepsilon_{\text{true}} - \varepsilon_t| \tag{12}$$

with the axial component $\varepsilon_{\text{true}}$ and the transverse component ε_t where ε_{dil} is the dilatational strain and ε_{dev} the deviatoric strain. Following this separation the final dimensions of the deformed samples were used to determine the ε_{dev} and ε_{dil}. The result is plotted in Fig. 17. At constant density the data of ε_{dev}, and at pure densification the data of ε_{dil} should lie on the diagonal line and the other parameter should be zero. According to Fig. 17 both ε_{dev} and ε_{dil} are important in the regime investigated here. Up to $\varepsilon_{\text{true}} \approx 30\%$ the densification

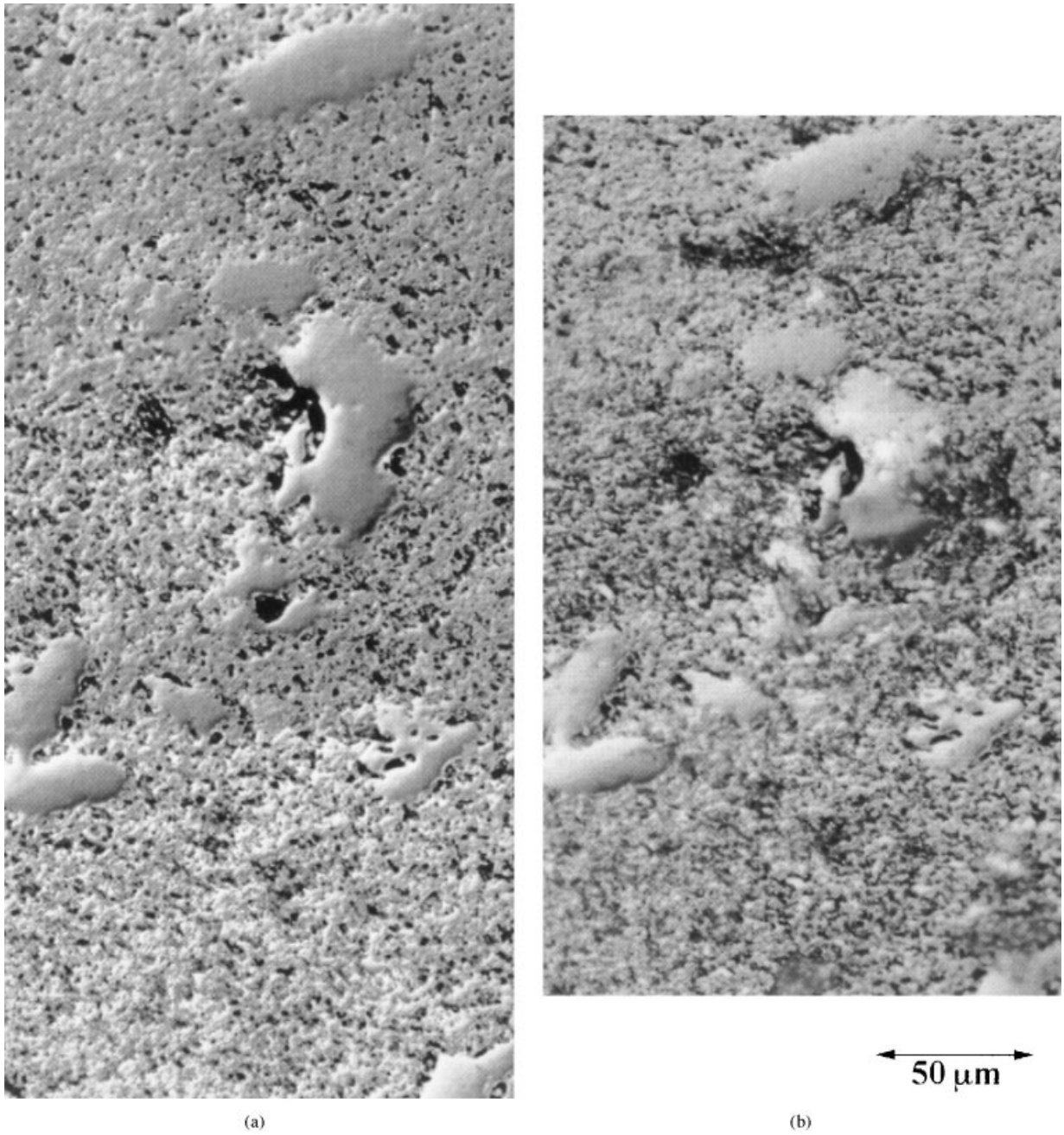

Fig. 15. Optical micrograph of the surface of the same specimen area (a) before and (b) after deformation at 1600°C for about 17% at 2×10^{-5} 1/s. The compression (and plastic forming) was applied in the vertical direction.

by compression has a larger contribution than the plastic deformation. At higher strains $|\varepsilon_{dil}|$ is more or less constant with a value of about 25%, while ε_{dev} increases linearly with ε_{true}. Reaching a constant value of ε_{dil} and a linear increase of ε_{dev} implies that a maximum density is achieved at $\varepsilon_{true} \approx 30\%$. At strains higher than 30% the material deforms mainly plastically.

3.4 Flow stress

In summary precursor-derived Si–B–C–N ceramics exhibit a pronounced increase of the apparent flow stress with deformation analogous to the decreasing strain rates in creep experiments with precursor-derived Si–C–N[24–27] and Si–B–C–N ceramics.[24,25] This change in the deformation behavior can be due to geometrical reasons like changes of sample size, and porosity and/or due to structural changes such as changes in the amorphous structure, phase separation and/or crystallization.

One geometrical reason for an increased apparent flow stress is—at constant strain rate—the increased effective strain rate at high strains. The decrease in porosity increases the apparent flow stress as well. The dependence of the flow stress on porosity[54,55] may be approximated by $(1-P)^2$ where P is the volume fraction of porosity. Combining the effects of porosity and change in sample size, using eqn (4) and assuming an otherwise

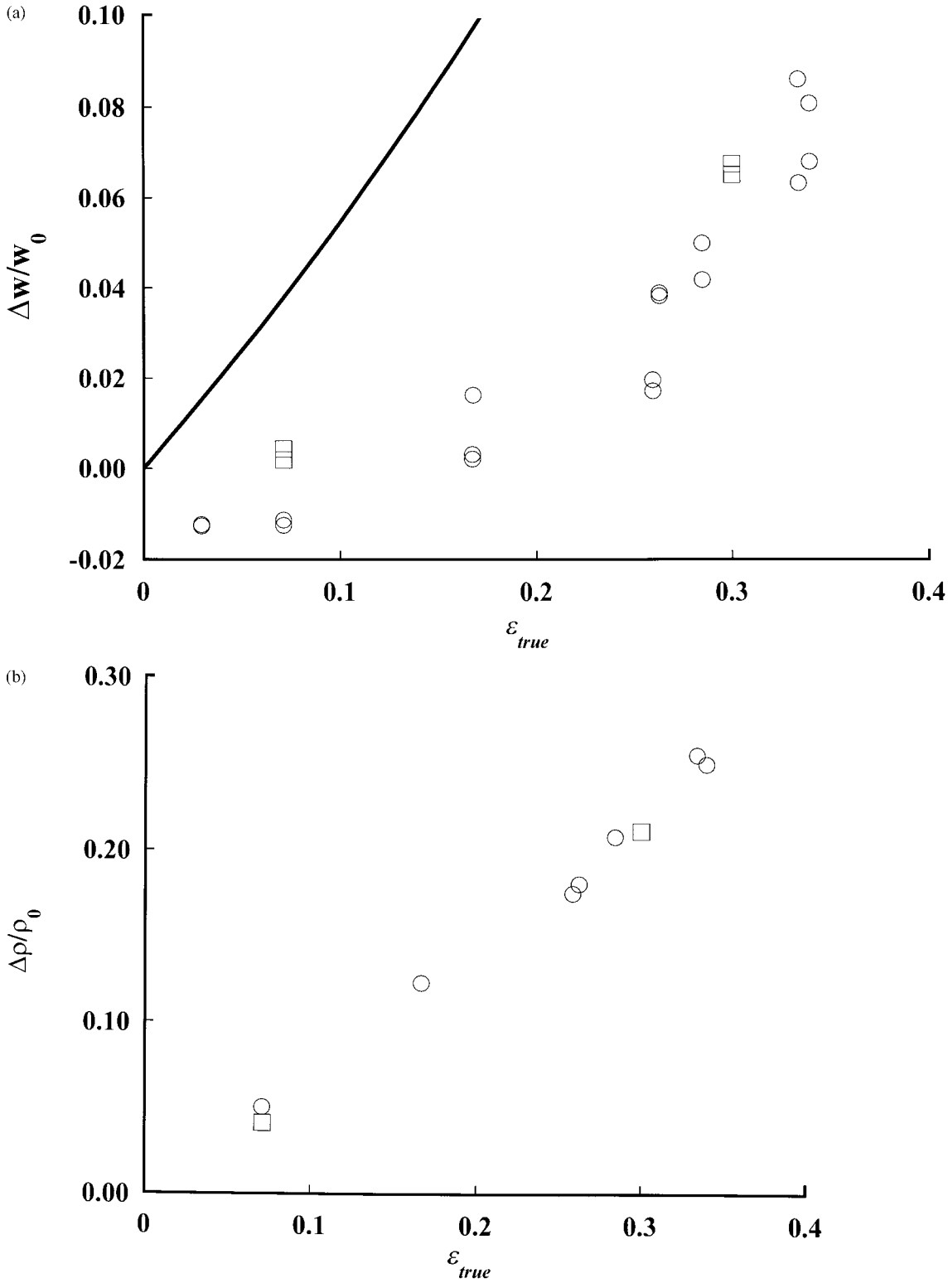

Fig. 16. Dependence of the relative change of (a) sample width $\Delta w/w_0$ and (b) density $\Delta\rho/\rho_0$ on true strain ε_{true} at 1500 (□) and 1600°C (○). The line in (a) is the dependence assuming a constant sample volume.

constant intrinsic structure the apparent flow stress σ_{app} can be formulated as

$$\sigma_{app} = \sigma_0 \left[\frac{1-P}{1-P_0}\right]^2 \left[\frac{l}{l_0}\right]^{1/n} \left[\frac{w}{w_0}\right]^2 \qquad (13)$$

with the original flow stress σ_0 and the sample length l and width w (the index zero in this formula marks the value before the test). Using the results shown in Fig. 16(a) and (b) and assuming 450 MPa for σ_0 the apparent flow stress as a function of deformation was computed for different values of n (Fig. 18). In comparison with a typical stress-strain curve a very good agreement is found for $n = 0{\cdot}5$ (...) which, however, is physically not reasonable. Plots with reasonable stress exponents like $n = 1$ (△) or 2 (□) demonstrate that changes of the

sample size and porosity are not responsible alone for the increase of the apparent flow stress but structural reasons must be taken into account as well.

Devitrification could be one reason. However, as discussed in Section 3.2, at 1500°C there was no crystallization observed and at 1600°C the relative volume amount of crystallites is too small for direct interaction between crystallites and therefore such interaction can be excluded as an explanation for the increase of flow stress. However, devitrification may influence the deformation by an other mechanism even if the relative volume fraction of crystallites is small. One possibility is the reduction of the effective volume of the flowing amorphous matrix. For amorphous alloys with small crystals this is well known.[56,57] In order to consider this

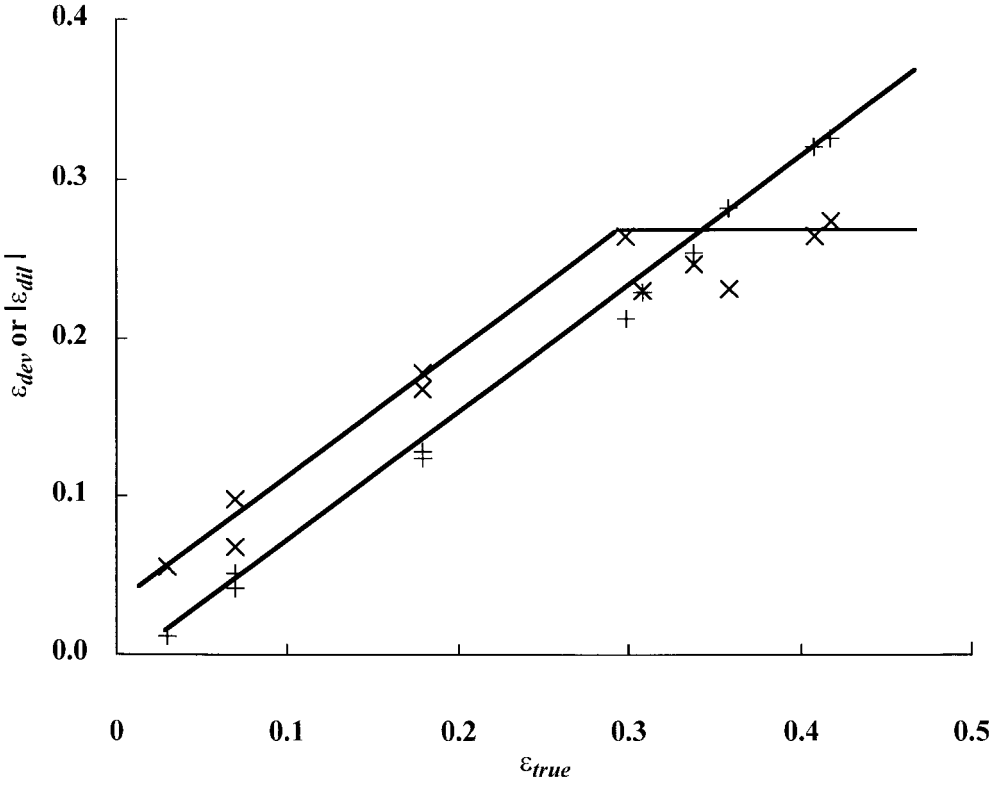

Fig. 17. Separation of the deviatoric strain ε_{dev} (+), which corresponds to plastic deformation and of the dilatational strain ε_{dil} (X), which relates to the volume change according to Refs 52 and 53.

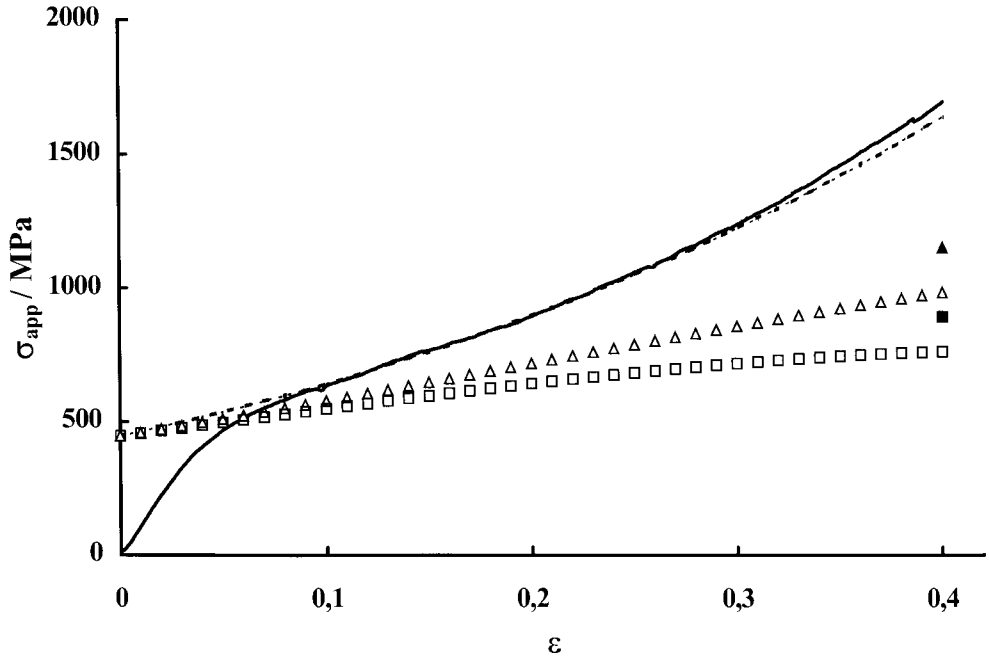

Fig. 18. Apparent increase in flow stress due to the change of sample size and porosity assuming constant flow stress ($\sigma_0 = 450$ MPa) calculated with eqn (13) in comparison with an experimental curve at 1600°C ($\dot{\varepsilon} = 4 \times 10^{-5}$1/s). The stress exponents used for calculation are $n = 0{\cdot}5$ (...), 1(△) and 2(□). The filled symbols include the effect of crystal growth according to Ref. 58.

effect a correction of eqn (4) by the factor $(1 - V_i)^{2+n/2}$ with the volume fraction of inclusion V_i was suggested by Ref. 58. Assuming $V_i = 10\%$ at $\varepsilon = 40\%$ this correction results in just a minor increase in flow stress as evidenced by the filled symbols in Fig. 18, not sufficiently high to explain the difference to the experimental data.

A second type of structural change could be changes in the amorphous structure itself. As argued in Refs 45–47, the structure of vitreous Si–C–N is very similar to those of the crystalline phases of the constituent elements. It consists of SiX_4 tetrahedra (X = C and/or N) forming three-dimensional networks in which each tetrahedron is attached to four neighboring tetrahedra. However, where in the crystalline state the network of the tetrahedra is periodic, the vitreous state lacks long-range periodicity and contains some free volume to accommodate the structural imperfections. The vitreous state thus corresponds to the so-called random network models, first proposed by Zachariasen[59] and accepted as the best description of the structure of vitreous or fused silica. It can be expected that in a similar way the B-containing vitreous quaternary ceramics consist of networks of short-range ordered polyhedra as well. Due to such structural similarities the amorphous materials under investigation can be considered as glass-type materials and their plastic flow as viscous flow.

Viscous flow is defined by

$$\dot{\varepsilon} = \frac{\sigma}{\eta} \tag{14}$$

with the viscosity η. According to simple rate theory,[60] a stress dependence of η can be formulated as

$$\frac{1}{\eta} \propto \frac{1}{\sigma} \sinh\left(\frac{V'\sigma}{2kT}\right) \tag{15}$$

with the activation volume V'. At small stresses the hyperbolic sine can be approximated with its argument resulting in the well known Newtonian case [with $n = 1$ in eqn (4)] with a viscosity independent of stress. At large stresses eqn (15) can be approximated by

$$\dot{\varepsilon} = \dot{\varepsilon}_0 \exp\left(\frac{V'\sigma}{2kT}\right) \tag{16}$$

where V' is equal to four times the apparent activation volume V of eqn (9).

For technical glasses Newtonian behavior usually is observed.[61] Exceptions are known for alkali borate glasses with the start of flow after a certain flow stress. Furthermore, non-Newtonian flow was observed for soda lime glasses under high stress which was attributed to structural rearrangements.[62] In the case of well-stabilized $Pd_{82}Si_{18}$ samples the non-Newtonian behavior was explained with the high stress case, i.e. eqn (16).[63] The hyperbolic sine dependence of eqn (15) most probably is the reason for the conflicting results of values for the stress exponent in the literature and in the present work. In the literature, Newtonian behavior with $n = 1$[27] or $n = 0{\cdot}7$[24] is reported for Si–C–N ceramics. As discussed above, the present investigation suggest non-Newtonian behavior with values of n bigger than 2. The experiments in Refs 24 and 27 were performed at stresses below 100 MPa and probably can be considered to obey the small stress approximation whereas the present results were determined at much higher stresses in the range of 250 to 2000 MPa.

As outlined above the relative amount of free volume of pore free amorphous material is estimated to be 22%. The authors suggest a model where the individual free volume sites are the rate-controlling flow defects which usually are assumed to be responsible for the viscous flow in amorphous material.[34,60] In this model individual tetrahedra or clusters of tetrahedra jump into neighboring free volume sites. Assuming such thermally activated jumps the apparent activation volume is a product of the cross section of the cluster (≈ cross section of the free volume site) and the jump distance. Since the jump distance is approximately equal to the diameter of the cluster the activation volume should be in the order of the jumping cluster. Fig. 19 shows the values of the apparent activation volume of Si–B–C–N amorphous materials in dependence on strain, calculated following eqn (9). It is clear that the apparent activation volume V decreases strongly with deformation from 2·5 to about 0·2 nm^3, but is not very sensitive to temperature. Values of apparent activation volume in the same order were found in metallic glasses[64,65] and glassy amorphous polymers.[66,67] Preliminary results from positron annihilation experiments on amorphous Si–B–C–N indicate also free volume sites in that size range (H. Schaefer, pers. comm.). Structures in the order of 1 to 5 nm were found by HADF imaging (see Fig. 7) and could also be interpreted as free volume sites in that order of size. Therefore, it is suggested that free volume sites are the basic unit in the thermal activation process and act as flow-defects. Then, the reduction of the apparent activation volume is due to the decrease of the size of free volume sites and thus of the shear distance. Most probably, this size decrease of the free volume sites is not directly related to deformation but due to sintering during testing at high temperatures.

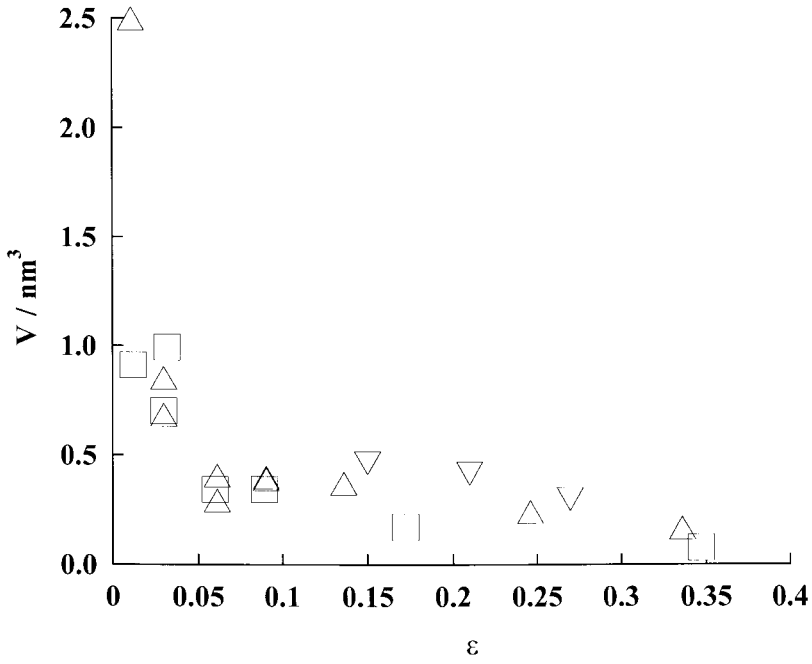

Fig. 19. Apparent activation volume derived from stress relaxation experiments according to eqns (7) and (9) depending on strain and temperature (□: 1500°C, △: 1600°C and ▽: 1650°C).

The apparent activation energy is 0·8 MJ mol^{-1} as shown earlier in Section 3.1 which is comparable to the self-diffusion energy of Si and C in SiC.[68] This value is large compared to the results of creep experiments on precursor-derived Si–C–N ceramics.[24–26] In these creep experiments the temperature dependence of creep rates suggests a much smaller activation energy (250 kJ mol^{-1}).[24–26] It is worthwhile to note that these experiments were performed at small strains ($<3\%$). At such small strains the present results exhibit almost no dependence of the stress on temperature and on strain rate, suggesting also a very small apparent activation energy. It is likely that in this regime the deformation is dominated by densification. Therefore, the different results of activation energy are due to different deformation regimes. In the regime of densification the deformation must be explained with an athermal process; at larger strains, i.e. larger stresses due to higher density, the material deforms predominantly via the free volume mechanism with an apparent activation energy of 0·8 MJ mol^{-1}.

A further reason for the increase in flow stress during deformation could be compositional changes in the metastable amorphous state during heat treatment as was found with ternary Si–C–N.[45–47] There, a phase separation into amorphous C and amorphous Si_3N_4 has been found which should result in a change of the viscosity of the decomposed material. Thus further investigations are necessary in order to determine whether similar phase transformations occur in quaternary material as well and could account for a change of the flow stress of the amorphous state.

4 Conclusions

High temperature compression tests on precursor-derived Si–B–C–N ceramics have demonstrated an impressive deformability of the glassy-type as-thermolysed material. Despite the high testing temperature only minor evidence was found for changes in composition and microstructure implying a remarkable stability of the amorphous state of the material investigated. A major part of the deformation is related to the densification (at least 26%) of the porous material. At true strains larger than about 30% no more densification was achieved and further deformation should be attributed to viscous flow only.

The stress necessary for densification at small strains is rather low. However, due to densification and structural changes in the amorphous state the apparent flow stress increases to the order of 2 GPa. In other words, after densification precursor-derived Si–B–C–N ceramics are rather creep resistant even at 1600°C.

The increase in apparent flow stress could not unambiguously be explained. Substantial changes are clearly due to the change in sample size and porosity. However, not all of the increase in flow stress can be attributed to these mechanisms; thus structural changes, like the decrease of the size of free volume, should be considered also. The value of the apparent activation volume and its decrease from 2·5 to 0·2 nm^3 suggest that free volume of that size range is responsible for the plastic deformation. Crystallization plays only a minor role in the deformation behavior, since only a small volume fraction crystallizes.

The good deformability is promising for the production of structural parts from precursor-derived ceramics, which are stable at very high temperatures. The high creep resistance at high temperatures of densified and heat-treated material further emphasises the prospect for future applications.

Acknowledgements

The experiments were performed at the Japan Science and Technology Corporation in Nagoya whose support is gratefully acknowledged. Furthermore, the authors are indebted to M. Weinmann for synthesizing the material and to S. Honda for his assistance in the mechanical testing. The authors would like to thank M. Christ for supplying the density data and M. Kaiser and his group for the chemical analysis. The thermodynamic calculations of H. Seifert and J. Peng are highly appreciated. I W. Chen is also sincerely acknowledged for his help in developing eqn (13).

References

1. Popper, P., *Brit. Ceram. Res. Assn. Special Publ.*, 1967, **57**, 1.
2. Verbeek, W. German patent 2218960, 1973.
3. Verbeek, W. Winter, G. German patent 2236078, 1974.
4. Winter, G. Verbeek, W. Mansmann, M. German patent 2243527, 1974.
5. Yajima, S., Hayashi, J. and Omori, M. *Chem. Lett.*, 1975, 931.
6. Yajima, S. Okamura, K. Hayashi. J. *Chem. Lett.*, 1975, 1209.
7. Yajima, S., Hayashi, J., Omori, M. and Okamura, K., *Nature*, 1976, **261**, 683.
8. Takamizawa, M. Kobayashi, T. Hayashida, A. Takeda, Y. US patent 4550151, 1985.
9. Takamizawa, M. Kobayashi, T. Hayashida, A. Takeda, Y. US patent 4604367, 1986.
10. Seyferth, D. and Plenio, H., *J. Am. Ceram. Soc.*, 1990, **73**(7), 2131.
11. Baldus, H.-P., Wagner, O. and Jansen, M., *Mat. Res. Soc. Symp. Proc.*, 1992, **271**, 821.
12. Funayama, O. Arai, M. Aoki, H. Tashiro, Y. Katahata, T. Sato, K. Isoda, T. Suzuki, T. Kohshi, I. US patent 5128286, 1992.
13. Funayama, O., Kato, T., Tashiro, Y. and Isoda, T., *J. Am. Ceram. Soc.*, 1993, **76**, 717.
14. Su, K., Remsen, E. E., Zank, G. A. and Sneddon, L. G., *Chem. Mater.*, 1993, **5**, 547.
15. Bill, J., Frieß, M., Aldinger, F. and Riedel, R., *Mat. Res. Soc. Symp. Proc.*, 1994, **346**, 605.
16. Bill, J. Kienzle, A. Sasaki, M. Riedel, R. and Aldinger, F. Novel routes for the synthesis of materials in the quaternary system Si–B–C–N and their characterization. In *Advances in Science and Technology 3B, Ceramics: Charting the Future*, ed. P. Vincenzini. Techna Srl., 1995, pp. 1291–1299.
17. Riedel, R., Kienzle, A., Dressler, W., Ruwisch, L., Bill, J. and Aldinger, F., *Nature*, 1996, **382**, 797.
18. Rice, R., *Am. Ceram. Soc. Bull.*, 1983, **62**, 916.
19. Seyferth, D. and Wiseman, G. H., *J. Am. Ceram. Soc.*, 1984, **67**, C–132.
20. Peuckert, M. and Vaahs, T., *Brück, Adv. Mater.*, 1990, **398**, 2.
21. Bill, J. and Aldinger, F., Precursor-derived covalent ceramics. *Adv. Mater.*, 1995, **7**, 775–787.
22. Baldus, H.-P. and Jansen, M., *Angew. Chem. Int. Ed. Engl.*, 1997, **36**, 328.
23. Baufeld, B. Wakai, F. and Honda, S., Mechanical properties of Si–B–C–N precursor-derived ceramics. In *6th International Symposium on Ceramic Materials and Components for Engines*, 19–23 October 1997, ed. K. Niihara, S. Kanzaki, K. Komeya, S. Hirano, and K. Morinaga. Arita, Japan, 1998, pp. 277–382.
24. Thurn, G. and Aldinger, F. Compression creep behaviour of precursor-derived ceramics. In *Precursor-derived covalent ceramics*; ed. J. Bill, F. Wakai and F. Aldinger. Wiley-VCH Verlag, Weinheim, 1999, pp. 237–245
25. Thurn, G., Canel, J., Bill, J., Aldinger, F., Compression creep behavior of precursor-derived Si–C-ceramics. *J. Eur. Cer. Soc.*, submitted for publication.
26. Bill, J., Seitz, J., Thurn, G., Dürr, J., Canel, J., Janos, B. Z., Jalowiecki, A., Sauter, D., Schempp, S., Lamparter, H. P., Mayer, J. and Aldinger, F., Structure analysis and properties of Si–C–N ceramics derived from polysilazanes. *Phys. Stat. Sol.*, 1998, **166**, 269–296.
27. An, L., Riedel, R., Konetschny, C., Kleebe, H.-J. and Raj, R., Newtonian viscosity of amorphous silicon-nitride at high temperature. *J. Am. Ceram. Soc.*, 1998, **81**(5), 1349–1352.
28. Bill, J. and Aldinger, F., Progress in materials synthesis. *Z. Metallkd.*, 1996, **87**, 827–884.
29. Kirby, P. L., Kinetics of mechanical relaxation processes. In *Inorganic Glasses in Non-Crystalline Solids*, ed. V. D. Frechette. John Wiley and Sons, New York, 1960, p. 269.
30. Vitek, V. Atomic structure and defects in metallic glasses: relationship of physical and mechanical properties. In *Plastic Deformation of Amorphous and Semi-crystalline Materials*, ed. B. Escaig, and C. G'Sell. Les Ulis, Les Editions de Physique, 1982, pp. 143–161.
31. Gilman, J. J., Mechanical behavior of metallic glasses. *J. Appl. Phys.*, 1975, **46**(4), 1625–1633.
32. Cohen, M. H. and Turnbull, D., *J. Chem. Phys*, 1959, **31**, 1164.
33. Turnbull, D. and Cohen, M. H., *J. Chem. Phys*, 1961, **34**, 120.
34. Spaepen, F. In *Physics of Defects*, ed. R. Balian *et al.* Les Houches Lectures XXXV, 1980, pp. 135–174
35. Weinmann, M., Haug, R., Bill, J., Aldinger, F., Schumacher, J. and Müller, K., Boron-containing polysilylcarbodi-imides: A new class of molecular precursors for Si–B–C–N ceramics. *J. Organomet. Chem.*, 1997, **541**, 345.
36. Seitz, J. and Bill, J., Production of compact polysilazane-derived Si/C/N-ceramics by plastic forming. *J. Mat. Sci. Let.*, 1996, **15**, 391–393.
37. Weinmann, M. Haug, R. Bill, J. DeGuire, M. and Aldinger, F., Boron-modified polysilylcarbodi-imides as precursors for Si–B–C–N ceramics: synthesis, plastic forming and high temperature behavior, *Appl. Organomet. Chem.*, 1998, **12**(10/11), 725–734.
38. Kaiser, G., Meyer, A., Friess, M., Riedel, R., Harris, M., Jacob, E. and Tölg, G., Critical comparison of ICP-OES, XRF and fluorine volatilization-FTIR spectrometry for the reliable determination of the silicon main constituent in ceramic materials. *Fresenius J. Anal. Chem.*, 1995, **352**, 318–326.
39. Egerton, R. F., *Electron Energy-Loss Spectroscopy in the Electron Microscope*. Plenum Press, New York, 1995.
40. Kasper, B. Phasengleichgewichte im system B–C–N–Si. Ph. D. thesis, Stuttgart, 1996.
41. Kasper, B., Seifert, H. J., Kußmaul, A., Lukas, H. L. and Aldinger, F., Entwicklung eines thermodynamischen Datensatzes fr das System B–C–N–O–Si. Werkstoffwoche 96, Symp. 7, pp. 623–628.

42. Cowley, J. M., *Diffraction Physics*. North-Holland, Amsterdam, 1981.
43. Spence, J. C. H., *Experimental High-Resolution Electron Microscopy*, 2nd edn. Oxford University Press, New York, 1988.
44. Colliex, C. and Mory, C. In *Quantitative Electron Microscopy*, ed. J. N. Chapman and A. J. Craven, Scottish Universities Summer School in Physics, 1984, p. 149.
45. Dürr, J., Schempp, S., Lamparter, P., Bill, J., Steeb, S. and Aldinger, F., X-ray neutron small angle scattering with Si–C–N ceramics using isotopic substitution. *Solid State Ionics*, 1997, **101–103**(1–4), 1041–1047.
46. Dürr, J. Ph.D. thesis, Stuttgart, 1997.
47. Schempp, S., Dürr, J., Lamparter, P., Bill, J. and Aldinger, F., Study of the atomic structure and phase separation in amorphous Si–C–N ceramics by X-ray and neutron diffraction. *Z. Naturforsch., A: Phys. Sci.*, 1998, **53**(3/4), 127–133.
48. Evans, A. G. and Rawlings, R. D., The thermally activated deformation of crystalline materials. *Phys. Stat. Sol.*, 1969, **34**, 9.
49. Langdon, T. G., Dependence of creep rate on porosity. *J. Am. Ceram. Soc.*, 1972, **55**, 630–631.
50. Hasselman, D. P. H., Porosity dependence of the elastic moduli of polycrystalline refractory materials. *J. Am. Ceram. Soc.*, 1962, **45**, 452–453.
51. Nishimura, T. Haug, R. Bill, J. Thurn, G. and Aldinger, F. Mechanical and thermal properties of Si–C–N-material from polyvinylsilazane. *J. Mat. Sci.*, 1998, **33**(21), 5237–5241.
52. Raj, R., Separation of cavitation-strain and creep-strain during deformation. *J. Am. Ceram. Soc.*, 1982, **65**(3), C46.
53. Venkatachari, K. R. and Raj, R., Shear deformation and densification of powder compacts. *J. Am Ceram. Soc.*, 1986, **69**(6), 399–406.
54. Kingery, W. D., *Introduction to Ceramics*. John Wiley and Sons, New York, 1960 p. 598.
55. Chen, W-I., Superplastic flow of two-phase alloys. In *International Conference on Superplasticity*, Grenoble, 16–19 September 1985. Editions due C.N.R.S., Paris, 1985, pp. 5.1–5.10.
56. Kim, Y. H., Inoue, A. and Masumoto, T., *Trans. Japan Inst. Metals*, 1990, **31**, 747.
57. Inoue, A., Horio, Y., Kim, H. and Masumoto, T., *Mater. Trans. Japan Inst. Metals*, 1992, **33**, 669.
58. Yoon, C. K. and Chen, I-W., Superplastic flow of two-phase ceramics containing rigid inclusions–zirconia/mullite composites. *J. Am. Ceram. Soc.*, 1990, **73**, 1555–1565.
59. Zachariasen, W. H., *J. Am. Chem. Soc.*, 1932, **54**, 3841.
60. Glasstone, S., Laidler, K. J. and Eyring, H., *The Theory of Rate Processes*. McGraw–Hill, New York, 1941 p. 480–486, 513–514.
61. Scholz, H. and Kreidl, N. J. In *Glass Science and Technology, Vol. 3, Viscosity and Relaxation*, ed. D.R. Uhlmann, N. J. Kreidl. 1986, p. 240.
62. Simmons, J. H., Mohr, R. K. and Montrose, C. J., Non-Newtonian viscous flow in glass. *J. Appl. Phys.*, 1982, **53**(6), 4075–4080.
63. Taub, A. I., *Acta. Met.*, 1980, **28**, 633.
64. Bobrov, O. P., Safonov, I. A. and Khonik, V. A., Low-temperature stress relaxation and activation volume in metallic glasses. *Phys. Solid State*, 1994, **36**(6), 931–934.
65. Deng, D., Zheng, F., Xu, Y., Qi, G. and Argon, A. S., Creep and structural relaxation in Pd40Ni40P20 glass. *Acta Metall. Mater*, 1993, **41**, 1089–1107.
66. Brady, T. E. and Yeh, G. S. Y., Yielding behavior of glassy amorphous polymers. *J. of Applied Physics*, 1971, **42**(12), 4622–4630.
67. Lefebvre, J. M. and Escaig, B., Plastic deformation of glassy amorphous polymers: influence of strain rate. *J. of Materials Science*, 1985, **20**, 438–448.
68. Kirschstein, G. and Koschel, D., *Gmelin, Handbook of Inorganic Chemistry, Si, Supplement Volume B2, Silicon Carbide Part 1*, 8th edn. Springer, Berlin, 1984 p. 107.